# Electronic Supplementary Information (ESI)

## Multicoated composites of nano silicon and graphene nanoplatelets as anodes in Li-ion batteries

Pin-Yi Zhao [a,b], Antonio Ruiz Gonzalez [a,b], Bing Li [a], Yu-Han Liu [b,c], Robert Palgrave [b], and Kwang-Leong Choy [a,*]

[a] Institute for Materials Discovery, University College London, 120-124 Roberts Building, London, WC1E 7JE, United Kingdom

[b] Department of Chemistry, University College London, 20 Gordon Street, London, WC1H 0AJ, United Kingdom

[c] Department of Physics and Astronomy, University College London, Gower Street, London, WC1E 6BT, United Kingdom

*Corresponding author. E-mail address: k.choy@ucl.ac.uk

## Table of contents

## Experimental

*Dispersant Selection*

The initial precursor was formulated by dispersing graphene nanoplatelets (particle size ~25 μm, with a specific surface area 50 to 80 $m^2/g$, Sigma-Aldrich) and nano silicon (Skyspring Nanomaterials, average particle size ~30 nm, USA) into the solvents to screen the most appropriate one. In this study, we tested: acetone, ultrapure water, ethanol, N-methylpyrrolidinone, acetonitrile, and ethyl acetate for the AACD deposition. The dispersion/solution was: (1) ultrasonicated for 0.5 h; (2) magnetically stirred (500 rpm, ~24 h); (3) settled still for *ex-situ* sedimentations.

The surface wetting properties of the substrate (spacer) were tested by an optical tensiometer (Attension Lite, tilted cradle) through sessile drop experiments. The tensiometer would analyze the shape for the contact angles. The image of the drop was acquired by a camera after an equilibrium state was achieved. The contact angle was assessed for the sample (average of 5 times).

*Electrode Fabrication*

Initially, the graphene nanoplatelets and nano silicon powder were distributed in N-methylpyrrolidinone (NMP, Alfa Aesar) in the listed concentration (see Table S1). Poly(vinylidene difluoride) (PVDF, Alfa Aesar) was pre-dissolved in NMP. The mass ratio of the total active mass to PVDF was 8:1. The dispersion was ultrasonicated for 1 h, after which magnetically stirred for ~24 h at 500 rpm.

Secondly, a glass slide (cleaned by VacuLAB, tantec) was placed beneath the spacer (MTI Corporation) to avoid contamination. An NMP mixture containing well-dispersed graphene

nanoplatelets and nano silicon was delivered to the pneumatic atomizer operated using compressed air as the carrier gas. The precursor mixture was deposited onto a heated substrate at 80 °C using the setup as shown in Figure 1a. The working distance between the substrate and the atomizer was kept at circa 20 cm. The atomizer was scanned at circa 20 cm $s^{-1}$ over the substrate and circa. 100 deposition cycles were used to build up the multicoated composite anode.

The compositions of the films were varied by tailoring the mass ratios of graphene nanoplatelets and nano silicon. The ratio of nano silicon/(graphene nanoplatelets+nano silicon) was varied from 0.05 (GNS5), 0.10 (GNS10), 0.20 (GNS20), to 0.30 (GNS30), as displayed in Table S1.

**Table S1.** Anode compositions and notations

| Notation | Concentration of graphene nanoplatelets (mg/mL) | Concentration of nano silicon (mg/mL) |
|---|---|---|
| GNS5 | 0.95 | 0.05 |
| GNS10 | 0.90 | 0.10 |
| GNS20 | 0.80 | 0.20 |
| GNS30 | 0.70 | 0.30 |

*Materials characterization*

The temperature distribution of the heated substrate was obtained through a forward-looking infrared (FLIR) camera (T335) after the thermal equilibrium of the substrate for 2 h. The cross-section morphology of the deposited film was characterized by the scanning electron microscope (SEM, ZEISS EVO LS15). Au layer (10 nm) was coated on the electrode by Q150R ES rotary-pumped sputter coater to counter charging effects, then the electrodes were

equipped with a conductive bridge. Powder X-ray diffraction (PANalytical X'Pert PRO, Bragg−Brentano geometry) with Cu $K_\alpha$ radiation source (40 kV, 40 mA) was operated at 2 theta of [10°, 80°] and 0.05° $s^{-1}$. Raman spectra were obtained using Renishaw inVia™ confocal Raman microscope of 514.5 nm excitation at 50 mW. X-ray photoelectron spectroscopy (XPS) spectra were obtained using a monochromatic Al-Ka X-ray source (energy = 1486.71 eV) on a Thermo Fisher K-Alpha spectrophotometer. The samples were positioned with regard to the analyser at the electron take-off angle normal to the surface. Each sample was subjected to a survey spectrum in the region 0–1050 eV (pass energy = 200 eV), followed by high-resolution measurements (pass energy = 50 eV) of Si 2p core levels. Thermogravimetric analysis (TGA, PerkinElmer, model 4000) was performed in air and $N_2$ within [30, 940] °C at a heating rate of 10 °C $min^{-1}$. The differences in the mass of the samples were then recorded at each employed temperature.

*Cell assembly*

After overnight drying in the vacuum oven (Thermo Scientific, VT6025) at 120 °C, the multicoated electrodes were delivered to an Ar-loaded glovebox (LABmaster pro SP) with $H_2O$ and $O_2$ <0.1 ppm. The mass of the electrode was calculated by the mass difference between the final electrode and the bare substrate. The typical mass loading of the electrode was ~0.2 mg $cm^{-2}$. CR2032 coin cells (MTI) were assembled in the glovebox and sealed through a crimping machine (MSK-110, MTI) at 850 psi. The counter electrode was a lithium metal disk. The separator was glass microfiber (Whatman, GF/B) soaked in LP30 electrolyte (1 M $LiPF_6$ in ethylene carbonate and dimethyl carbonate, volume ratio 1:1). No expensive electrolyte additives were adopted.

*Electrochemical characterizations*

The constant-current discharge/charge, cycling stability, and rate capability tests were performed using a battery test station (Neware) at ambient temperature (~21.0 °C). All testing voltage range was within 0.05 to 2 V unless otherwise specified. The specific capacity was evaluated based on the total mass of active materials. Cyclic voltammetry (CV) was conducted at 0.1 mV $s^{-1}$ scan rate on an MPG-2 potentiostat (Biologic). The Galvano electrochemical impedance spectra were obtained with an alternating current (AC) of 0.1 mA in the range of frequency from $10^6$ to 0.01 Hz ambiently (~21.0 °C) by the Gamry (Interface 1010E). Rate capability was obtained after cycling performance.

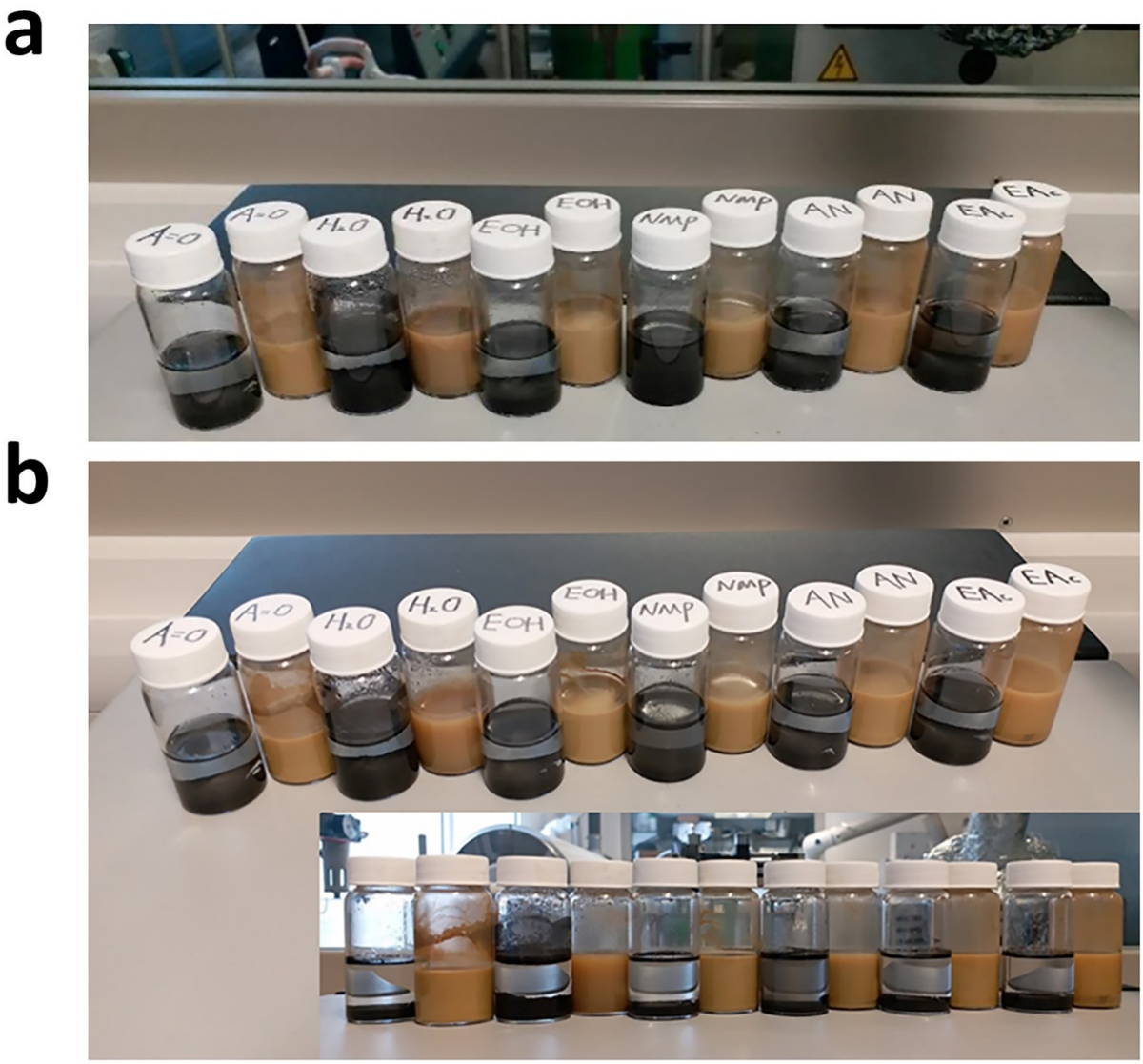


**Figure S1.** Dispersion test of graphene nanoplatelets and nano silicon in several common solvents: acetone (A=O), ultrapure water ($H_2O$), ethanol (EOH), N-methylpyrrolidinone (NMP), acetonitrile (AN), and ethyl acetate (EAc) after sedimentation for (a) ~72 h, and (b) ~168 h (the inset displays another perspective)

Solvent's ability to withstand aggregation and/or sedimentation was tested to establish the dispersive stability of graphene nanoplatelets and nano silicon. Acetone, ultrapure water, ethanol, N-methylpyrrolidinone, acetonitrile, and ethyl acetate were tested as potential solvents. The resulting samples were observed after 72 and 168 hours. Figure S1.a shows the outcome after sedimentation (~72 h). It is shown that NMP exhibits the best dispersion for

graphene nanoplatelets, while ethyl acetate ranks in second place. For nano silicon, there is little visual discrepancy among various solvents. Figure S1.b illustrates the results after ~168 h sedimentation. Also, for graphene nanoplatelets, NMP keeps the best stability, while graphene nanoplatelets in other solvents are all sedimented. No distinct dissimilarity is observed on the nano silicon side. Given the opening choice on the graphene nanoplatelets, the solvent would both select NMP for consistency.

The wetting property of NMP on the substrate was determined by the optical tensiometer and displayed in Figure S2. The obtained contact angle was the average value after 10 s apparent equilibrium, with error generally within ± 2°. It is shown that the advancing angle is 40.85° with a hysteresis of 0.62°. The result shows that NMP spreads over (<90°) [1] the surface of the spacer, with a contact angle of ~40°.

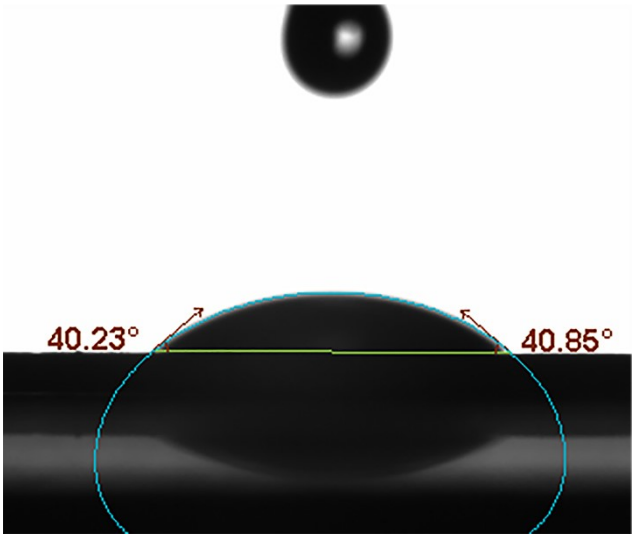


**Figure S2.** The contact angle of NMP on the spacer

Intuitively, high-temperature substrates will accelerate the evaporation of the solvent during the deposition, shortening the time needed for the fabrication. Since the use of a high deposition temperature would cause intense solvent evaporation which is likely to introduce cracking in the deposited film [2], therefore, the substrate temperature was chosen at 80 °C, which is one of the initial drying temperatures adopted in battery research [3, 4]. This temperature is also supported by TGA in the following discussion.

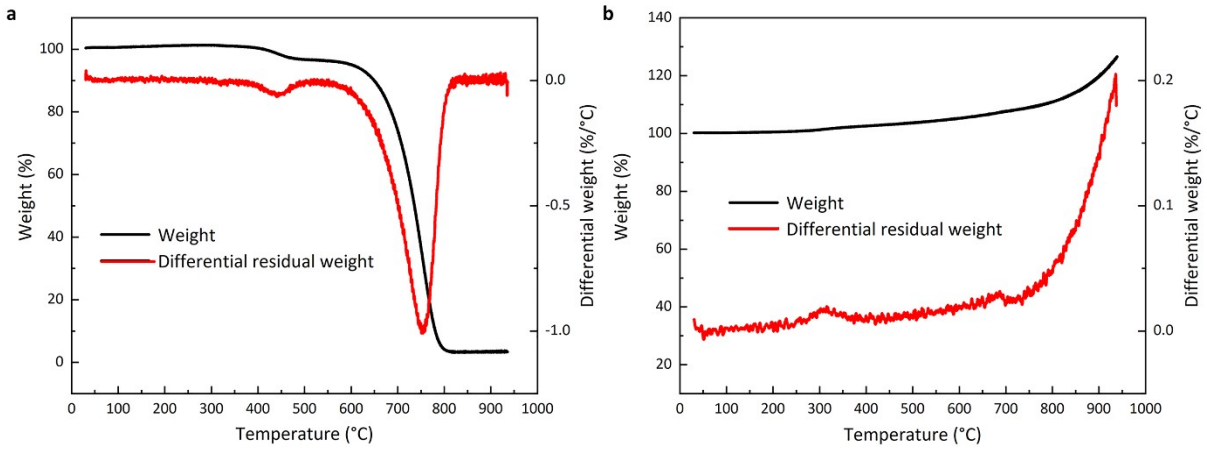


**Figure S3.** TGA and differential TGA curves in the air of (a) graphene nanoplatelets and (b) nano silicon

TGA in the air (Figure S3) reveals that the weight of graphene nanoplatelets and nano silicon increased trivially in the air (0.68% and 0.27%, respectively) within the full operation range (120 °C). Silicon has a very thin protective layer of $SiO_2$ on its surface and oxidation in the air (product: $SiO_2$) starts at 950 °C while reaction with $N_2$ begins at 1400 °C [5]. In Figure S3.b, silicon delivers a lower starting temperature of reaction due to features of nanomaterials [6]. Meanwhile, the TGA in the air could reveal the oxide content of silicon.

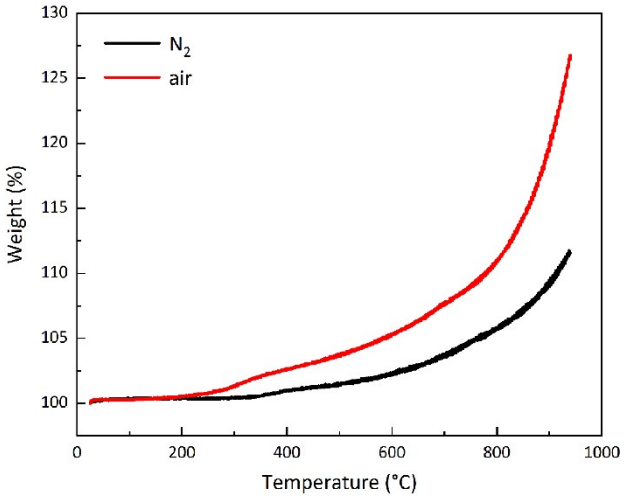


**Figure S4.** TGA curve of nano silicon in air and $N_2$

Analysis of nano silicon purity:

Considering nano silicon sample (total weight: $m_0$) with a certain ratio of impurity $SiO_2$ (impurity ratio: $a$). Therefore, the weight of $SiO_2$ is $am_0$, and the mass of pure nano silicon ( $m_1$) is

$$m_1 = (1 - a)m_0 \tag{1}$$

Ideally, all the silicon nanopowder ($m_1$) is oxidized to $SiO_2$ ($m_2$) after sintering. The ratio of weight increase is ($m_1$ and $m_2$ shares the same chemical amount):

$$r_1 = \frac{m_2 - m_1}{m_1} \times 100\% = \frac{60 - 28}{28} \times 100\% = 114\% \tag{2}$$

However, the ratio of weight increase from the experiment is $r_2$ ($r_2 \leq r_1$) as a result of the $SiO_2$ impurity ($am_0$). Consider the weight increase contributed by nano silicon,

$$r_1 m_1 = r_2 m_0 \tag{3}$$

Therefore, the impurity ratio

$$a = \left(1 - \frac{m_1}{m_0}\right) \times 100\% = (1 - r_2/r_1) \times 100\% = \frac{r_1 - r_2}{r_1} \times 100\% \tag{4}$$

To deconvolute weight contribution by $N_2$ and $O_2$ (assuming only the two components of air are the source of weight gain), TGA was conducted on nano silicon powder in air and $N_2$ (Figure S4). Reaching the upper limit of the equipment, the difference between the residual weight percentage (in air and $N_2$) was approaching 14% (e.g., 930.5 °C, 13.9%), which is the contribution of weight increase on nano silicon by $O_2$. In this case $r_2 = 113.9\%$, thus

$$a = \frac{r_1 - r_2}{r_1} \times 100\% = \frac{114\% - 113.9\%}{114\%} \times 100\% < 0.1\% \quad (5)$$

It shows that the raw material of nano silicon is very pure in terms of oxidation, and the electrochemical activity of $SiO_2$ is omitted, which is consistent with the report [7]. We then directly applied nano silicon void of further treatments (e.g., functionalization) to better detach the effect of concentration from other variables.

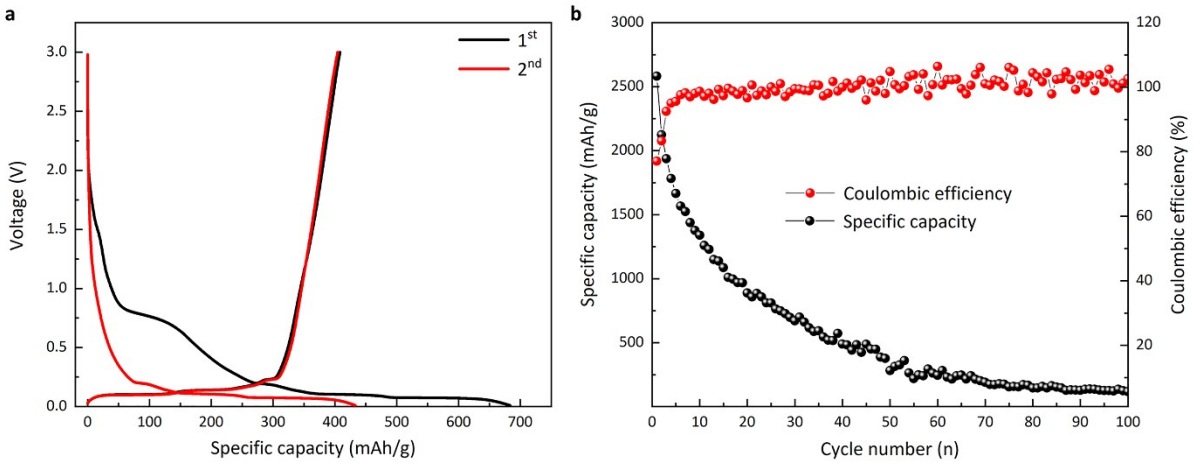


**Figure S5.** (a) Initial two cycles of graphene nanoplatelets at the current density of 37.2 mA/g, [0.05, 3] V, and (b) cycling stability of nano silicon anode at 0.36 A/g, [0.05, 2] V. Both (a) and (b) are doctor bladed to check the electrochemical performance of the raw materials

Experiments for data in Figure S5:

Figure S5. (a): graphene nanoplatelets (Sigma Aldrich, 80 wt.%), PVDF (Alfa Aesar, 10 wt.%), and superP (Timcal, 10 wt.%); (b) nano silicon powder (Skyspring Nanomaterials, USA, 60 wt.%), PVDF (Alfa Aesar, 20 wt.%), and superP (Timcal, 20 wt.%) was blended with NMP (Alfa Aesar) to get slurry. The slurry was doctor-bladed (wet thickness: 200 μm) on Cu foil. The prepared film was (1) baked at 80 °C for 5 h, (2) baked overnight at 120 °C in vacuum, (3) sliced into Φ = 12.7 mm electrodes, (4) baked at 120 °C in vacuum, and (5) transferred to an argon-filled glovebox.

The electrochemical behavior of raw materials (graphene nanoplatelets and nano silicon) was evaluated separately at the beginning by constant-current discharge/charge. Figure S5.a displays the initial two cycles of graphene nanoplatelets at 37.2 mA/g within the potential

interval of [0.05, 3] V. The graphene nanoplatelets have a specific charge capacity of ~400 mAh $g^{-1}$ with a soft carbon electrochemical behavior during the primary two cycles, less than the debated expectation (such as $Li_2C_6$ or $Li_3C_6$ [8, 9]) of graphene. In this case, the theoretical limit of the graphene nanoplatelets is perceived as 372 mAh $g^{-1}$ (denoted as $Q_1$). Figure S5.b is the cycling stability of nano silicon anode at 0.36 A/g within [0.05, 2] V. The cut-off potential was set to fully release the capacity of nano silicon as well as maintaining the cycling stability and mitigating volume change [10-12]. The average particle size of nano silicon is ~30 nm (reported from the manufacturer) and well below the critical particle size of fracture (150 nm) under volume change [13] but larger than a reported optimized size (5 nm) [14]. The charge capacity fades quickly within 100 cycles with a starting point higher than 2500 mAh $g^{-1}$. The initial specific capacity agrees that nano silicon is a promising high-capacity material. Thus, the theoretical limit of the nano silicon adopts ambient value, 3579 mAh $g^{-1}$ (denoted as $Q_2$) [15, 16].

The theoretical limit of the composite electrodes: GNS5, GNS10, GNS20, and GNS30, is obtained by a weighted average (eq.1 and eq.2):

$$Q_{composite} = w_1 Q_1 + w_2 Q_2 \quad (1)$$

$$w_1 + w_2 = 1 \quad (2)$$

where $Q_{composite}$ represents the theoretical specific capacity of the composite, $Q_1$ is the theoretical limit of the graphene nanoplatelets with a weight percentage $w_1$, and $Q_2$ is the theoretical limit of nano silicon with a weight percentage $w_2$. By applying the two equations, the theoretical specific capacity of composites studied in this work could be calculated (Table

S2). These theoretical specific capacity values are displayed as dashed lines in Figure 3e-h and indicate an upper limit of the electrochemical performance.

**Table S2.** The theoretical limit of the composite electrodes tested within the present work

| Composite | Theoretical limit $(mAh/g)$ |
|---|---|
| $Q_{GNS5}$ | 532.35 |
| $Q_{GNS10}$ | 692.7 |
| $Q_{GNS20}$ | 1013.4 |
| $Q_{GNS30}$ | 1334.1 |

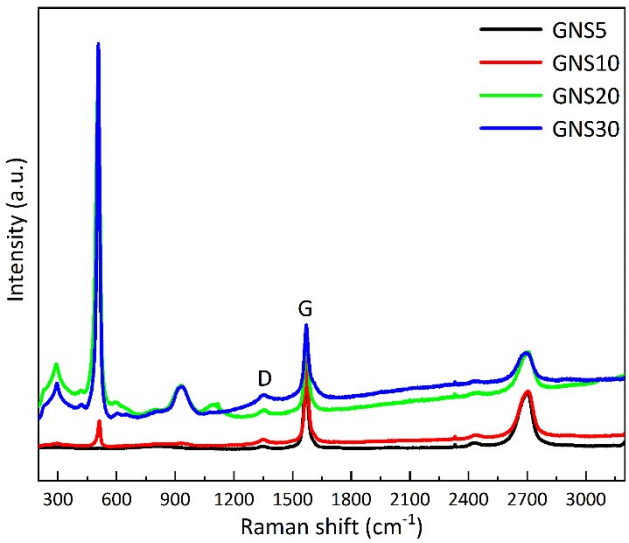


**Figure S6.** Raman spectra of GNS5, GNS10, GNS20, and GNS30

The 1st and 2nd order transversal optical modes are shown by a strong signal at ~520 $cm^{-1}$ and a weaker signal at ~900 $cm^{-1}$, respectively [17]. Carbons display relevant D and G modes. The G band is substantially sharper than the D band, suggesting the existence of graphite which is consistent with report [18-19]. Meanwhile, an evident peak centred on ~2683 $cm^{-1}$ was found, which is strongly associated with graphene layers [20].

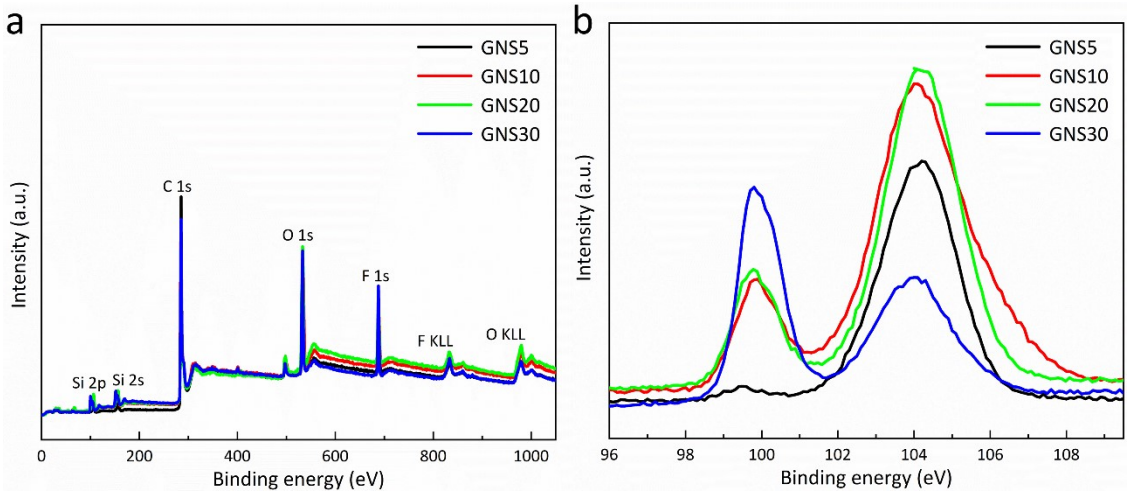


**Figure S7.** (a) X-ray photoelectron spectroscopy (XPS) of GNS5, GNS10, GNS20, and GNS30, (b) high-resolution Si 2p XPS spectrum

The entire XPS spectrum is shown, which includes Si, C, O, and F components in Figure S7a. Figure S7b shows the high-resolution Si 2p XPS spectrum. The 99.7 eV peak is attributed to Si-Si bonding, indicating the existence of silicon in the composite [20]. The signal at 104 eV is Si-O bonding on the surface, indicating that fresh nano silicon particles may be partly oxidised during manufacture.

**Presentation for cyclic discharge and charge pattern**

It is facile to directly obtain continuous discharge/charge patterns between specific capacity and potential through galvanostatic cycling with potential limitation (GCPL) techniques. While in some other circumstances without a direct presentation, basic transforms such as (1) axisymmetric, and (2) horizontal translation are manually applied to the 'X-type' discharge/charge patterns. Through geometric and algebraic operations, it is demonstrated that approach two is the simplified algorithm. The obtained continuous pattern facilitates visualization between discharge and charge curves especially within one cycle, while the movement among different individual cycles clearly shows the trend of capacity fading.

The first-cycle data is easier to process given that only the charge curve is transformed. From the second cycle, the discharge/charge pattern needs to be processed by both (1) axisymmetric, and/or (2) translational transform. Data of the specific capacity is listed as a column vector while cycle number is denoted in subscript and cycle status (discharge or charge) is denoted as superscript ('d' for discharge and 'c' for charge). For example, the specific capacity of the $n^{th}$ cycle ($n \in N^*$) discharge data is denoted as the vector: $X_n^d$. The last-row element (row number: j) of $X_n^d$ is frequently adopted as the symmetric axis ($x = a_{n,j}^d$) in geometric axisymmetric transformations. Note that the geometric transformations (non-bold) have been combined with algebraic operations (**bold**). During algebraic operation, row numbers in subscript (1, 2, 3, ...*i*... *j*) do not change within a specific discharge/charge. Given that $A_n$ and $B_n$ are column vectors, in which each row there is only one constant, the row number of $A_n$ and

$B_n$ would be adjusted accordingly to satisfy operation rules within themselves and with $X_n$ and $Y_n$. **0** denotes the zero vector.

Approach one:

(1) axisymmetric transformation on the charge curve

The charge curve ($X_n^c$) is geometrically transformed over an axis $x = a_{n,j}^{\ d}$ to get $X_{n'}^{\ c}$:

$$X_{n'}^{\ c} = 2A_n^d - X_n^c = 2\begin{bmatrix} a_{n,\,j}^{\ d} \\ \vdots \\ a_{n,\,j}^{\ d} \end{bmatrix} - \begin{bmatrix} (X_n^c)_1 \\ (X_n^c)_2 \\ \vdots \\ (X_n^c)_j \end{bmatrix} = \begin{bmatrix} 2a_{n,\,j}^{\ d} - (X_n^c)_1 \\ 2a_{n,\,j}^{\ d} - (X_n^c)_2 \\ \vdots \\ 2a_{n,\,j}^{\ d} - (X_n^c)_j \end{bmatrix} \tag{1}$$

$A_n^d$ is a column vector (row is *j*), each row there is only one constant element: $a_{n,j}^{\ d}$. The last-row element (row number: *j*) of $X_{n'}^{\ c}$ is denoted as $a_{n',j}^{\ c}$.

(2) translational transformation on both discharge/charge curves

A. translational transformation on the charge curve

$$X_{n}^{\ c}{}_{,,} = X_{n}^{\ c}{}_{,} - \left(A_{n}^{\ c}{}_{,} - A_n^d\right) = \begin{bmatrix} 2a_{n,\,j}^{\ d} - (X_n^c)_1 \\ 2a_{n,\,j}^{\ d} - (X_n^c)_2 \\ \vdots \\ 2a_{n,\,j}^{\ d} - (X_n^c)_j \end{bmatrix} - \left( \begin{bmatrix} a_{n,\,j}^{\ c}{}_{,} \\ \vdots \\ a_{n,\,j}^{\ c}{}_{,} \end{bmatrix} - \begin{bmatrix} a_{n,\,j}^{\ d} \\ \vdots \\ a_{n,\,j}^{\ d} \end{bmatrix} \right) = - \begin{bmatrix} (X_n^c)_1 \\ (X_n^c)_2 \\ \vdots \\ (X_n^c)_j \end{bmatrix} + \begin{bmatrix} 3a_{n,\,j}^{\ d} - a_{n,\,j}^{\ c}{}_{,} \\ \vdots \\ 3a_{n,\,j}^{\ d} - a_{n,\,j}^{\ c}{}_{,} \end{bmatrix}$$

$$= -X_n^c + 3A_n^d - A_{n'}^c \tag{2}$$

$A_{n'}^c$ is a column vector (row number is *j*), each row there is only one constant: $a_{n',j}^{\ c}$.

Note that $\left(a_{n',j}^{\ c}, 0\right)$ corresponds to the origin of the Cartesian basis XY before axisymmetric transformation,

$$A_{n}^{\ c}{}_{,} = 2A_n^d - 0 = 2A_n^d \tag{3}$$

Therefore

$$X_{n''}^{c} = -X_n^c + 3A_n^d - A_{n}^{c'} = -X_n^c + 3A_n^d - 2A_n^d = A_n^d - X_n^c = \begin{bmatrix} a_{n,\,j}^{\ d} \\ \vdots \\ a_{n,\,j}^{\ d} \end{bmatrix} - \begin{bmatrix} (X_n^c)_1 \\ (X_n^c)_2 \\ \vdots \\ (X_n^c)_j \end{bmatrix} = \begin{bmatrix} a_{n,\,j}^{\ d} - (X_n^c)_1 \\ a_{n,\,j}^{\ d} - (X_n^c)_2 \\ \vdots \\ a_{n,\,j}^{\ d} - (X_n^c)_j \end{bmatrix} \tag{4}$$

Now the newly combined $n^{th}$ cycle U-shape curve (denoted as $Y_n$, row number $i$+$j$, $n \in N^*, n \geq 2$) composed of discharge curve ($X_n^d$ the row number of which is $i$) and charge curve ($X_{n''}^{c}$ the row number of which is $j$) is continuous. The vector is

$$Y_n = \begin{bmatrix} X_n^d \\ X_{n''}^{c} \end{bmatrix} = \begin{bmatrix} (X_n^d)_1 \\ (X_n^d)_2 \\ \vdots \\ (X_n^d)_i \\ (X_{n''}^{c})_{i+1} \\ (X_{n''}^{c})_{i+2} \\ \vdots \\ (X_{n''}^{c})_{i+j} \end{bmatrix} \tag{5}$$

B. translational transformation of the above $Y_n$ to $Z_n$

The last-row element (row number: $i$+$j$) of $Y_1$ is denoted by $b_{1,i+j}$. $B_1$ is an (i+j)-row column vector, in which each row there is only one constant: $b_{1,i+j}$. Similarly, the last-row element (row number: $i$+$j$) of $Z_n$ is denoted by $c_{n,i+j}$ ($n \in N^*, n \geq 2$). $C_n$ is an (i+j)-row column vector, in which each row there is only one constant: $c_{n,i+j}$.

Obviously, $Y_1$ does not need a translation. Thus

$$Z_1 = Y_1 \tag{6}$$

Accordingly, the second-cycle translation is based on the first cycle:

$$Z_2 - Y_2 = \begin{bmatrix} (Z_2)_1 \\ (Z_2)_2 \\ \vdots \\ (Z_2)_i \\ (Z_2)_{i+1} \\ (Z_2)_{i+2} \\ \vdots \\ (Z_2)_{i+j} \end{bmatrix} - \begin{bmatrix} (X_2^d)_1 \\ (X_2^d)_2 \\ \vdots \\ (X_2^d)_i \\ (X_{2}^{c''})_{i+1} \\ (X_{2}^{c''})_{i+2} \\ \vdots \\ (X_{2}^{c''})_{i+j} \end{bmatrix} = \begin{bmatrix} (Z_2)_1 - (X_2^d)_1 \\ (Z_2)_2 - (X_2^d)_2 \\ \vdots \\ (Z_2)_i - (X_2^d)_i \\ (Z_2)_{i+1} - (X_{2}^{c''})_{i+1} \\ (Z_2)_{i+2} - (X_{2}^{c''})_{i+2} \\ \vdots \\ (Z_2)_{i+j} - (X_{2}^{c''})_{i+j} \end{bmatrix} = \begin{bmatrix} b_{1,\ i+j} \\ \vdots \\ \\ \\ \\ \\ \vdots \\ b_{1,\ i+j} \end{bmatrix} = B_1 \tag{7}$$

From the third cycle, the recursion is

$$Z_3 - Y_3 = \begin{bmatrix} (Z_3)_1 \\ (Z_3)_2 \\ \vdots \\ (Z_3)_i \\ (Z_3)_{i+1} \\ (Z_3)_{i+2} \\ \vdots \\ (Z_3)_{i+j} \end{bmatrix} - \begin{bmatrix} (X_3^d)_1 \\ (X_3^d)_2 \\ \vdots \\ (X_3^d)_i \\ (X_{3}^{c''})_{i+1} \\ (X_{3}^{c''})_{i+2} \\ \vdots \\ (X_{3}^{c''})_{i+j} \end{bmatrix} = \begin{bmatrix} (Z_3)_1 - (X_3^d)_1 \\ (Z_3)_2 - (X_3^d)_2 \\ \vdots \\ (Z_3)_i - (X_3^d)_i \\ (Z_3)_{i+1} - (X_{3}^{c''})_{i+1} \\ (Z_3)_{i+2} - (X_{3}^{c''})_{i+2} \\ \vdots \\ (Z_3)_{i+j} - (X_{3}^{c''})_{i+j} \end{bmatrix} = \begin{bmatrix} c_{2,\ i+j} \\ \vdots \\ \\ \\ \\ \\ \vdots \\ c_{2,\ i+j} \end{bmatrix} = C_2 \tag{8}$$

$$Z_4 - Y_4 = \begin{bmatrix} (Z_4)_1 \\ (Z_4)_2 \\ \vdots \\ (Z_4)_i \\ (Z_4)_{i+1} \\ (Z_4)_{i+2} \\ \vdots \\ (Z_4)_{i+j} \end{bmatrix} - \begin{bmatrix} (X_4^d)_1 \\ (X_4^d)_2 \\ \vdots \\ (X_4^d)_i \\ (X_{4}^{c''})_{i+1} \\ (X_{4}^{c''})_{i+2} \\ \vdots \\ (X_{4}^{c''})_{i+j} \end{bmatrix} = \begin{bmatrix} (Z_4)_1 - (X_4^d)_1 \\ (Z_4)_2 - (X_4^d)_2 \\ \vdots \\ (Z_4)_i - (X_4^d)_i \\ (Z_4)_{i+1} - (X_{4}^{c''})_{i+1} \\ (Z_4)_{i+2} - (X_{4}^{c''})_{i+2} \\ \vdots \\ (Z_4)_{i+j} - (X_{4}^{c''})_{i+j} \end{bmatrix} = \begin{bmatrix} c_{3,\ i+j} \\ \vdots \\ \\ \\ \\ \\ \vdots \\ c_{3,\ i+j} \end{bmatrix} = C_3 \tag{9}$$

…

$$Z_n - Y_n$$

$$= \begin{bmatrix} (Z_n)_1 \\ (Z_n)_2 \\ \vdots \\ (Z_n)_i \\ (Z_n)_{i+1} \\ (Z_n)_{i+2} \\ \vdots \\ (Z_n)_{i+j} \end{bmatrix} - \begin{bmatrix} (X_n^d)_1 \\ (X_n^d)_2 \\ \vdots \\ (X_n^d)_i \\ \left(X_n^{c''}\right)_{i+1} \\ \left(X_n^{c''}\right)_{i+2} \\ \vdots \\ \left(X_n^{c''}\right)_{i+j} \end{bmatrix} = \begin{bmatrix} (Z_n)_1 - (X_n^d)_1 \\ (Z_n)_2 - (X_n^d)_2 \\ \vdots \\ (Z_n)_i - (X_n^d)_i \\ (Z_n)_{i+1} - \left(X_n^{c''}\right)_{i+1} \\ (Z_n)_{i+2} - \left(X_n^{c''}\right)_{i+2} \\ \vdots \\ (Z_n)_{i+j} - \left(X_n^{c''}\right)_{i+j} \end{bmatrix} = \begin{bmatrix} c_{n-1,\ i+j} \\ \vdots \\ \vdots \\ \vdots \\ \vdots \\ \vdots \\ c_{n-1,\ i+j} \end{bmatrix} = C_{n-1}(n \in I$$

(10)

Approach two:

(1) axisymmetric and translational transformation on the charge curve

The charge curve ($X_n^c$) is horizontally translated by the length of $a_n^d$ first, then transformed over an axis $x = a_{n,j}^d$ to get $X_{n'}^c$:

$$X_{n'}^c = 2A_n^d - \left(X_n^c + A_n^d\right) = A_n^d - X_n^c = \begin{bmatrix} a_{n,\,j}^{\,d} \\ \vdots \\ \vdots \\ a_{n,\,j}^{\,d} \end{bmatrix} - \begin{bmatrix} (X_n^c)_1 \\ (X_n^c)_2 \\ \vdots \\ (X_n^c)_j \end{bmatrix} = \begin{bmatrix} a_{n,\,j}^{\,d} - (X_n^c)_1 \\ a_{n,\,j}^{\,d} - (X_n^c)_2 \\ \vdots \\ a_{n,\,j}^{\,d} - (X_n^c)_j \end{bmatrix} \tag{1}$$

Now the newly combined $n^{th}$ cycle U-shape curve (denoted as $Y_n$ row number $i$+$j$, $n \in N^*, n \geq 2$), composed of discharge curve ($X_n^d$ the row number is $i$) and charge curve ($X_{n'}^c$ the row number is $j$) is continuous. The vector is

$$Y_n = \begin{bmatrix} X_n^d \\ X_{n'}^c \end{bmatrix} = \begin{bmatrix} (X_n^d)_1 \\ (X_n^d)_2 \\ \vdots \\ (X_n^d)_i \\ (X_{n'}^c)_{i+1} \\ (X_{n'}^c)_{i+2} \\ \vdots \\ (X_{n'}^c)_{i+j} \end{bmatrix} \tag{2}$$

It is shown that approach two could reach the ($A_n^d - X_n^c$) more conveniently compared with approach one.

(2) translational transformation of the above $Y_n$

This recursion is similar to approach one.

$$Z_1 = Y_1 \tag{3}$$

$$Z_2 - Y_2 = B_1 \tag{4}$$

$$Z_3 - Y_3 = C_2 \tag{5}$$

$$Z_4 - Y_4 = C_3 \tag{6}$$

…

$$Z_n - Y_n = C_{n-1}\left(n \in N^*, n \geq 3\right) \tag{7}$$

It is shown above that in this operation the order of axisymmetric transformation and translational transformation could be exchanged while reaching the same results. However, approach two accelerates algebraic operations with a more conveniently obtained $Y_n$ and a simplified algorithm. Therefore, approach two could be considered as the simplified algorithm upon manual processing.

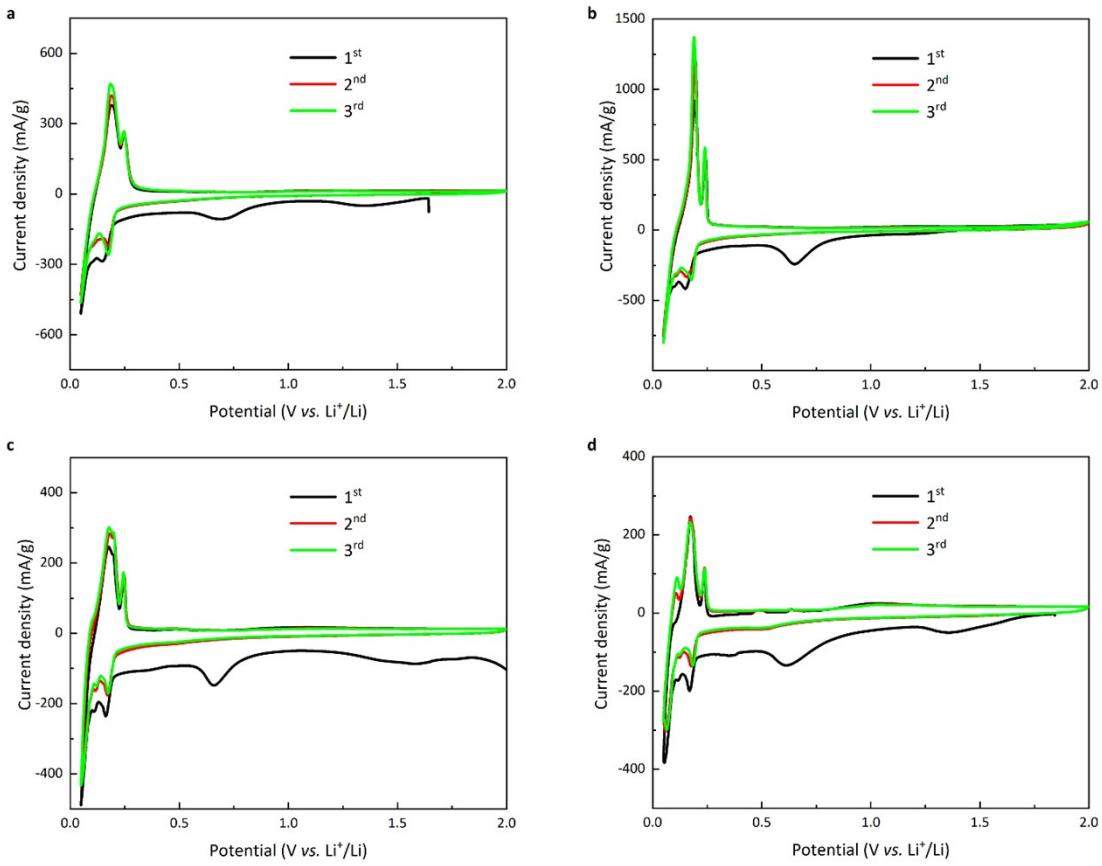


**Figure S8.** Cyclic voltammetry of the different composite materials tested at 0.1 mV $s^{-1}$ within [0.05, 2] V of (a) GNS5, (b) GNS10, (c) GNS20, and (d) GNS30

The 1st cathodic scan displays a wide peak between 1.0 V and 0.5 V, which is attributed to the formation of the solid electrolyte interface (SEI) on graphene nanoplatelets and silicon [21]. It is common practice for anodes to perform activation [22] and mitigate the high irreversibility, thus our analysis focuses on the following cycles. The cathodic peak at ~0.2 V originates from the formation of $Li_xSi$ ($x \leq 4.4$) [23]. Multilayer graphene component contributes the cathodic peak at ~0.10 V as well as the anodic peak at ~0.15 V and ~0.11 V while the cathodic peak at ~0 V is for both crystalline and amorphous silicon [24]. The 3rd cycle of the scan overlays well with the 2nd cycle of the scan, implying the favorable reversibility of the electrode [25].

**Table S3.** Comparison of the anode materials, fabrication methods, and electrochemical performances of nano silicon/graphene composite anodes

| Materials | Synthetic method | Current density and potential | Cycles | Performance (mAh $g^{-1}$) | Retention | Fulfilled ratio* | Rate | Reference |
|---|---|---|---|---|---|---|---|---|
| Si NP with graphene | Simple mixing | 0.1 A/g, 0.02-2 V | 20 | 600 | 30% | 28% | N/A | [26] |
| Si NP with rGO | punchy stirring | 50 mA/g, 0.01-1.5 V | 70 | 1261 | 56% | N-I | 200 mA/g, 1750 mAh/g | [27] |
| Si NP with GO (1:2) | freeze-drying | 0.18 A/g, 0.05-1.5 V | 100 | 786.3 | 103% | 50% | 1.8A/g, 600 mAh/g | [28] |
| Si NP with rGO | spray assisted method | 1C, 0.01-3 V | 50 | 1050 | 81% | 78% | 5C, 672 mAh/g | [29] |
| Si NP with graphene | aerosol spraying | 0.5 A/g, 0.002-1.5 V | 100 | 160 | 16% | N-I | 10C, 1000 mAh/g | [30] |
| Si NP with GO | vacuum filtration | 2A/g , 0.02-1 V | 200 | 500 | 33% | N-I | 4A/g, 750 mAh/g | [31] |
| Si NP with rGO | rotary evaporation | 50 mA/g, 2.0-0.075 V | 100 | 85 | 39% | 8% | N/A | [32] |
| Si NP with rGO | electrostatic self-assembly | 500 mA/g, 0.05-2 V | 50 | 1280 | 49% | N-I | 1 A/g, 880 mAh/g | [33] |
| Si NP with graphene sheets | mixing | 2 A/g, 0.02-1 V | 40 | 300 | 25% | N-I | 0.8 A/g, 600 mAh/g | [34] |
| GNS5 | AACD | 0.17 A/g, 0.05-2 V | 500 | 387.6 | 91% | 80% | 1.5 A/g, 185 mAh/g | This work |
| GNS10 | AACD | 0.17 A/g, 0.05-2 V | 500 | 425.2 | 86% | 72% | 1.5 A/g, 267 mAh/g | This work |

N/A indicates the data were not provided.
N-I indicates there is not sufficient information to calculate. *Fulfilled ratio on the next page.

$$Fulfilled\ ratio = Q_{isc}/Q_{tsc} \times 100\%$$

where $Q_{isc}$ represents initial specific charge capacity and $Q_{tsc}$ is the theoretical specific capacity. The fulfilled ratio quantifies the percentage achievement within a specific material design. What's more, it establishes a standard of comparison between different material designs where the fulfilled percentage is considered in addition to the absolute value.

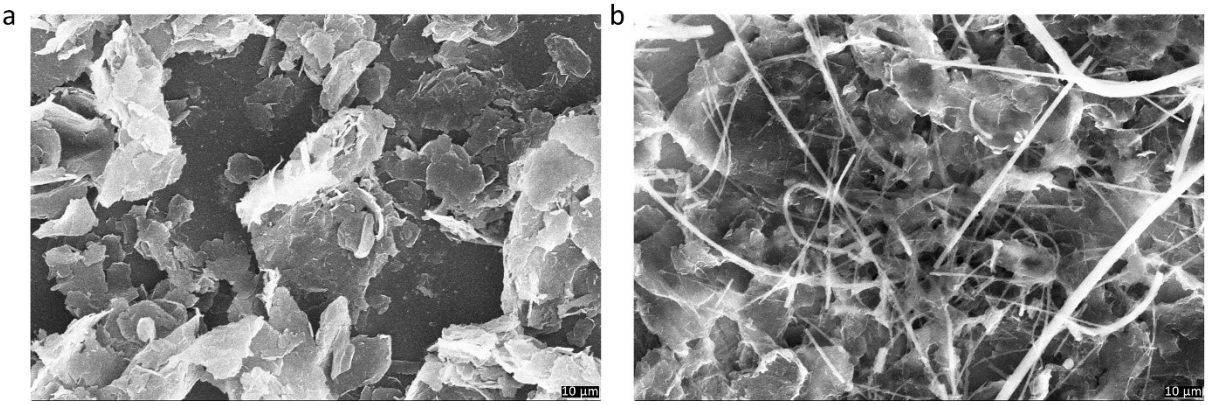


**Figure S9.** SEM of an electrode - GNS 10, (a) before and (b) after the cycling and rate tests

On the cycled electrode of GNS 10, SEM characterization was performed. The original form and structural integrity are still there, indicating outstanding structural stability. The electrode surface in Figure S9b has a morphology with no evident fracture or pulverisation, indicating that the material has good electrochemical stability, though a few glass fibers from the separator remain.

References


1. Atkins, P. and J.d. Paula, *Physical Chemistry Thermodynamics, Structure, and Change*. 2014: WH Freeman and Company New York.
2. Perednis, Dainius. Thin film deposition by spray pyrolysis and the application in solid oxide fuel cells. Diss. ETH Zurich, 2003.
3. Ueno, K., et al., *A design approach to lithium-ion battery electrolyte based on diluted solvate ionic liquids.* Journal of The Electrochemical Society, 2016. **164**(1): p. A6088.
4. Kim, D.S., Y.E. Kim, and H. Kim, *Improved fast charging capability of graphite anodes via amorphous $Al_2O_3$ coating for high power lithium ion batteries.* Journal of Power Sources, 2019. **422**: p. 18-24.
5. Greenwood, N.N. and A. Earnshaw, *Chemistry of the Elements*. 2012: Elsevier.
6. Bandyopadhyay, A.K., *Nano materials*. 2008: New Age International.
7. Bridel, J.-S., et al., *Key parameters governing the reversibility of Si/carbon/CMC electrodes for Li-ion batteries.* Chemistry of materials, 2010. **22**(3): p. 1229-1241.
8. Lu, J., et al., *High-performance anode materials for rechargeable lithium-ion batteries.* Electrochemical Energy Reviews, 2018. **1**(1): p. 35-53.
9. Bøggild, P., *The war on fake graphene*. 2018, Nature Publishing Group.
10. Li, J. and J. Dahn, *An in situ X-ray diffraction study of the reaction of Li with crystalline Si.* Journal of The Electrochemical Society, 2007. **154**(3): p. A156.
11. Obrovac, M. and L. Krause, *Reversible cycling of crystalline silicon powder.* Journal of the Electrochemical Society, 2006. **154**(2): p. A103.
12. Tornheim, A., S.E. Trask, and Z. Zhang, *Communication—Effect of Lower Cutoff Voltage on the 1st Cycle Performance of Silicon Electrodes.* Journal of The Electrochemical Society, 2019. **166**(2): p. A132.
13. McDowell, M.T., et al., *25th anniversary article: understanding the lithiation of silicon and other alloying anodes for lithium‐ion batteries.* Advanced Materials, 2013. **25**(36): p. 4966-4985.
14. Kim, H., et al., *A critical size of silicon nano‐anodes for lithium rechargeable batteries.* Angewandte Chemie International Edition, 2010. **49**(12): p. 2146-2149.
15. Obrovac, M. and V. Chevrier, *Alloy negative electrodes for Li-ion batteries.* Chemical reviews, 2014. **114**(23): p. 11444-11502.
16. Obrovac, M., et al., *Alloy design for lithium-ion battery anodes.* Journal of The Electrochemical Society, 2007. **154**(9): p. A849.
17. Krause, Andreas, et al. "In situ raman spectroscopy on silicon nanowire anodes integrated in lithium ion batteries." Journal of The Electrochemical Society 166.3 (2019): A5378.
18. Ruther, Rose E., et al. "Chemical evolution in silicon–graphite composite anodes investigated by vibrational spectroscopy." ACS applied materials & interfaces 10.22 (2018): 18641-18649.
19. Bøggild, Peter. "The war on fake graphene." (2018): 502-503.
20. Liu, Wen, et al. "Electrospray synthesis of nano-Si encapsulated in graphite/carbon microplates as robust anodes for high performance lithium-ion batteries." Sustainable Energy & Fuels 2.3 (2018): 679-687.
21. Wen, Y., et al., *Graphene‐bonded and‐encapsulated Si nanoparticles for lithium ion battery anodes.* Small, 2013. **9**(16): p. 2810-2816.
22. Jia, H., et al., *Hierarchical porous silicon structures with extraordinary mechanical strength as high-performance lithium-ion battery anodes.* Nature communications, 2020. **11**(1): p. 1-9.
23. Xia, M., et al., *$Ti_3C_2T$ x MXene Nanosheets as a Robust and Conductive Tight on Si Anodes Significantly*

*Enhance Electrochemical Lithium Storage Performance.* ACS nano, 2020. **14**(4): p. 5111-5120.

24. Chen, X., et al., *Conductive rigid skeleton supported silicon as high-performance Li-ion battery anodes.* Nano letters, 2012. **12**(8): p. 4124-4130.
25. Chang, J., et al., *Multilayered Si nanoparticle/reduced graphene oxide hybrid as a high‐performance lithium‐ion battery anode.* Advanced materials, 2014. **26**(5): p. 758-764.
26. Lee, Jeong K., et al. "Silicon nanoparticles–graphene paper composites for Li ion battery anodes." Chemical communications 46.12 (2010): 2025-2027.
27. Tang, H., et al. "Self-assembly silicon/porous reduced graphene oxide composite film as a binder-free and flexible anode for lithium-ion batteries." Electrochimica Acta 156 (2015): 86-93.
28. Chabot, Victor, et al. "Graphene wrapped silicon nanocomposites for enhanced electrochemical performance in lithium ion batteries." Electrochimica Acta 130 (2014): 127-134.
29. Azeemi, Rehman Yousuf, et al. "A simple spray assisted method to fabricate high performance layered graphene/silicon hybrid anodes for lithium-ion batteries." International Journal of Hydrogen Energy 44.36 (2019): 20267-20277.
30. Wen, Yang, et al. "Graphene-bonded and-encapsulated Si nanoparticles for lithium ion battery anodes." Small 9.16 (2013): 2810-2816.
31. Zhou, Min, et al. "High-performance silicon battery anodes enabled by engineering graphene assemblies." Nano letters 15.9 (2015): 6222-6228.
32. Botas, Cristina, et al. "Silicon-reduced graphene oxide self-standing composites suitable as binder-free anodes for lithium-ion batteries." ACS applied materials & interfaces 8.42 (2016): 28800-28808.
33. Chang, Peng, et al. "Constructing three-dimensional honeycombed graphene/silicon skeletons for high-performance Li-ion batteries." ACS applied materials & interfaces 9.37 (2017): 31879-31886.
34. Wang, Bin, et al. "Approaching the Downsizing Limit of Silicon for Surface-Controlled Lithium Storage." Advanced materials 27.9 (2015): 1526-1532.